

# Deep Implicit Statistical Shape Models for 3D Medical Image Delineation

Ashwin Raju

PAII Inc.

Bethesda, MD, USA

ashwinraju101@gmail.com

Shun Miao

PAII Inc.

Bethesda, MD, USA

Chi-Tung Cheng

Chang Gung Memorial Hospital

Linkou, Taiwan, ROC

Le Lu

PAII Inc.

Bethesda, MD, USA

Mei Han

PAII Inc.

Palo Alto, CA, USA

Jing Xiao

PingAn Insurance Group

Shenzhen, China

Chien-Hung Liao

Chang Gung Memorial Hospital

Linkou, Taiwan, ROC

Junzhou Huang

University of Texas at Arlington

Arlington, TX, USA

Adam P. Harrison

PAII Inc.

Bethesda, MD, USA

adam.p.harrison@gmail.com

## Abstract

3D delineation of anatomical structures is a cardinal goal in medical imaging analysis. Prior to deep learning, statistical shape models (SSMs) that imposed anatomical constraints and produced high quality surfaces were a core technology. Today’s fully-convolutional networks (FCNs), while dominant, do not offer these capabilities. We present deep implicit statistical shape models (DISSMs), a new approach to delineation that marries the representation power of convolutional neural networks (CNNs) with the robustness of SSMs. DISSMs use a deep implicit surface representation to produce a compact and descriptive shape latent space that permits statistical models of anatomical variance. To reliably fit anatomically plausible shapes to an image, we introduce a novel rigid and non-rigid pose estimation pipeline that is modelled as a Markov decision process (MDP). We outline a training regime that includes inverted episodic training and a deep realization of marginal space learning (MSL). Intra-dataset experiments on the task of pathological liver segmentation demonstrate that DISSMs can perform more robustly than three leading FCN models, including nnU-Net: reducing the mean Hausdorff distance (HD) by 7.7-14.3 mm and improving the worst case Dice-Sørensen coefficient (DSC) by 1.2-2.3%. More critically, cross-dataset experiments on a dataset directly reflecting clinical deployment scenarios demonstrate that DISSMs im-

prove the mean DSC and HD by 3.5-5.9% and 12.3-24.5 mm, respectively, and the worst-case DSC by 5.4-7.3%. These improvements are over and above any benefits from representing delineations with high-quality surfaces.

## 1. Introduction

3D segmentation is a fundamental task in medical imaging analysis. Currently, medical segmentation is dominated by fully-convolutional networks (FCNs) [26], which segment each pixel or voxel in a bottom-up fashion. This voxel-by-voxel approach is well-suited to the underlying convolutional neural network (CNN) technology and is both very straightforward and powerful to implement using modern deep learning software. The current state has been made particularly plain by the dominance of nnU-Net [16], i.e. “nothing-new U-Net”, in the medical segmentation decathlon (MSD) segmentation challenge [44]. Yet despite their undisputed abilities, FCNs do lack important features compared to prior technology. For one, a surface-based representation is usually the desired end product, but FCNs output voxel-based masks, which suffer from stair-like discretization effects (see top panel of Fig. 1). These are always deleterious, but are particularly severe when large inter-slice distances come into play. Conversion to a smoothed mesh is possible, but it introduces its own artifacts. While this is an important drawback, an arguably

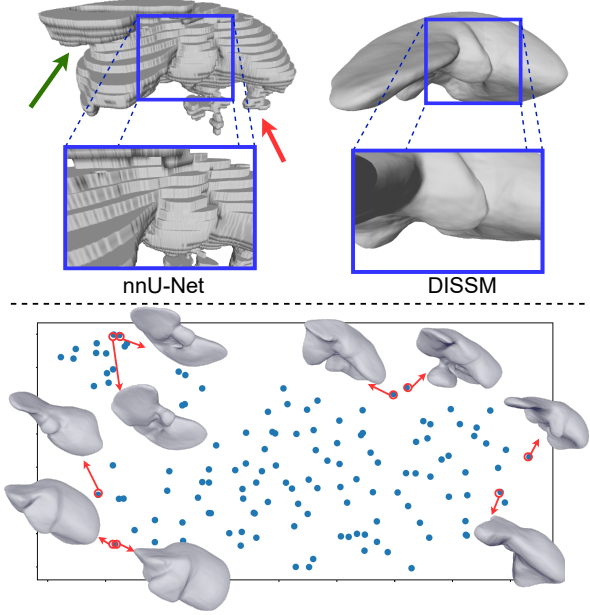


**Figure 1. Top Panel:** DISSMs produce high quality surfaces without mask-based discretization effects and use rich and explicit anatomical priors that allow it to perform robustly, even on highly challenging cross-dataset clinical samples. In this example, nnU-Net [16] oversegments the cardiac region (green arrow) and mishandles a TACE-treated lesion (red arrow), causing a fragmented effect. **Bottom Panel:** a 2D t-SNE embedding [46] of the DISSM shape latent space. Shapes closer together share similar features.

more critical limitation is that, on their own, FCNs offer no way to incorporate anatomical priors.

Shape priors are critical for ensuring anatomically plausible delineations, but current FCN pipelines typically operate with no shape constraints. This means that the techniques and concepts of statistical shape models (SSMs), so integral prior to deep learning [14], have fallen out of the mainstream. Despite the introvertive power of FCNs, the lack of anatomical priors can still lead them to occasionally produce egregious mistakes, especially when presented with morbidities, scanners, or other scenarios not seen in training (again see top panel of Fig. 1). It is likely impossible to capture all clinical scenarios well enough in training datasets. FCNs may also struggle with anatomical structures with low-contrast boundaries. Efforts have been made to incorporate some manner of anatomical priors with CNN technology [36, 41, 49, 40, 4, 33, 2], but these either do not directly model shape and/or do not estimate rigid poses, thus not producing a true SSM. Even should their interoperation with CNNs not be an issue, traditional SSMs also present their own distinct challenges, as they mostly rely on the point distribution model (PDM) [8], meaning they require determining a correspondence across shapes. Dense 3D surface landmarks are not typically pos-

sible to define, and even when so, they are not always reliably present [14]. The alternative of automatically generating correspondences is a dense research topic in its own [14], and all existing solutions are imperfect. Ideally, correspondences would not be required.

To fill these gaps, we introduce deep implicit statistical shape models (DISSMs), a new and deep approach to SSMs. Using the recently introduced deep implicit shape concept [37, 5, 30], DISSMs learn a compact and rich latent space, *e.g.*, size-256 latent vectors in our work, that can accurately and densely generate the signed distance functions (SDFs) of a representative sample of shapes. Importantly, correspondence between shapes is completely unnecessary, eliminating a major challenge with traditional SSMs. Statistics, *e.g.*, mean shape, principle components analysis (PCA), and interpolation, can be performed directly on the latent space (see bottom panel of Fig. 1). To fit an anatomically plausible shape to a given image, DISSMs use a CNN to determine rigid and non-rigid poses, thus marrying the representation power of deep networks with anatomically-constrained surface representations. Pose estimation is modelled as a Markov decision process (MDP), which iteratively determines a trajectory of rigid and non-rigid poses, where the latter are defined as PCA loadings of the DISSM latent space. To handle the intractably large search space of poses, DISSMs make use of marginal space learning (MSL) [51, 52] and inverted episodic training, the latter a concept we introduce. A final constrained deep level set refinement [31] corrects for any fine details not captured by the DISSM latent shape space. At a high level, DISSMs share many philosophies with traditional SSMs, but they modernize these concepts in a powerful deep-learning framework.

We apply DISSMs to the problem of 3D pathological liver delineation from computed tomography (CT) scans, comparing our approach to leading 2D [13], hybrid [24], and 3D cascaded [16] liver segmentation FCNs. When trained and tested on the MSD liver dataset [44], DISSMs provide more robust delineations, improving the mean Hausdorff distance (HD) by 7.7-14.3mm and the worst case Dice-Sørensen coefficient (DSC) performance by 1.2-2.3%, while matching or bettering mean values. *This is over and above any benefits of directly outputting a high resolution surface.* To further demonstrate robustness, we perform cross-dataset evaluation on an external dataset (97 volumes) designed to directly reflect clinical conditions [39], which is the target deployment scenario for delineation solutions. DISSMs improve the mean DSC and HD from 92.4% to 95.9% and from 34.1mm to 21.8mm, respectively, over the best alternative (nnU-Net [16]). Worst-case DSC is boosted from 88.1% to 93.4%. These results confirm the value, once taken for granted, of incorporating anatomical priors in 3D delineation. Our contributions are thus: 1) we are

the first to introduce a fully functioning *deep* SSM model that outputs high resolution surfaces; 2) we build a new correspondence-free, compact, and descriptive anatomical prior; 3) we present a novel pose estimation scheme that incorporates inverted episodic training and MSL; and 4) we provide a more robust solution than leading FCNs in both intra- and cross-dataset evaluations.

## 2. Related Work

**Anatomical Shape Priors:** Because anatomical structures are highly constrained, delineations can be constrained by shape priors. SSMs were at one point a workhorse for 3D medical segmentation and were most popularly realized as PDMs [8], which requires determining a set of surface point correspondences across all shapes. Correspondence permitted statistical techniques, such as PCA, to model shape variability [14]. Unfortunately, an explicit and dense surface parameterization is difficult to obtain and influences the final result. While PDMs have been used with CNNs [33, 2], these make no attempt at determining rigid poses, thus they are only applicable in constrained and limited setups. In general the reliance on explicit surface representations hinders the interoperation of traditional SSMs with CNN technology. SSMs based on level sets have been explored [9], but SDFs do not form a linear space for a valid PCA and the statistics must be collected across a densely sampled 3D regular grid. Another line of work use indirect voxel-based constraints by auto-encoders (AEs) [36, 41] or generative adversarial networks (GANs) [49, 40, 4], but these are hard to interpret and are not invariant to rigid similarity transforms, meaning a true shape prior is not constructed [14]. Recent work has investigated whether CNNs-based networks can output 3D mesh [50, 47] or point-cloud [4] segmentations by deforming an initial sphere, but this process is often used to augment an existing voxel-based output [50, 4], otherwise the deformation cannot capture all details [47]. More importantly, these works offer no means to incorporate anatomical priors. Like traditional SSMs, DISSMs explicitly enforce shape constraints via a model of anatomical variability based on PCA loadings, but using a deep implicit SDF *representation* that is 1) highly descriptive, 2) highly compact, and 3) requires no correspondences. DISSM is the first to offer a complete “deep” SSM solution that includes rigid and non-rigid pose estimation.

**Deep Implicit Shapes:** The concept of deep implicit shapes [37, 5, 30] were introduced to represent shapes using a compact latent space and an SDF decoder. DISSMs adopt Park *et al.*’s auto-decoder based formulation [37]. Unlike these seminal works, DISSMs builds a model of anatomical variability and fits the shape model to a given image using physical coordinates.

**Pose Estimation:** Fitting an SSM to an image requires determining the rigid and non-rigid poses of the shape. Stan-

dard learning strategies, such as one shot regression [45, 11] and exhaustive scanning [53], yield sub-optimal results as the model relies on a prohibitively large number of samples [12] and only has one opportunity to produce pose estimations. A recent work directly regresses poses using deep implicit shapes, but these are from simulated 2D images with white backgrounds [48]. DISSMs must operate in the challenging 3D medical setting, where datasets may be small and the contrast is low. Similar to deep reinforcement learning (DRL) [34], DISSMs model pose estimation as an MDP, where the agent navigates to a pose matching the present anatomical structure. Unlike DRL, and similar to recent registration approaches tasks [25, 21, 27], the loss can be directly calculated. However, estimating both non-rigid and rigid poses presents an extremely large search space. To deal with this, we introduce inverted episodic training. In addition, DISSMs employ MSL [52, 51], which incrementally learns pose parameters in the marginal spaces of lower dimension. The use of MSL links DISSMs to a variety of traditional SSM works pre-dating modern deep networks [52].

**FCN Refinements:** Although SSMs combined with reliable pose estimation can produce robust organ shapes, they can miss fine details. DISSMs use an FCN to refine the boundaries, incorporating components of a recently introduced level set loss [31] to retain the desired implicit SDF representation. FCN architectures [17, 32] for 3D medical images have been extensively studied.

## 3. Method

Fig. 2 illustrates the DISSM framework. As the bottom panel demonstrates, DISSMs use a CNN encoder to predict rigid and non-rigid poses, which, along with desired coordinates, are fed into a deep implicit multilayer perceptron (MLP) shape decoder to output corresponding SDF values. The encoder searches for the best pose using a MDP combined with MSL (top panel). We first outline the deep implicit shape model, discuss pose estimation, then describe the final local surface refinement.

### 3.1. Implicit Shape Representation

Deep implicit shapes [37, 5, 30] are a recent and powerful implicit shape representation. We use these technologies to model the distribution of organ shapes using an SDF representation, which, given a coordinate, outputs the distance to a shape’s surface:

$$SDF(\mathbf{x}) = s : x \in \mathbb{R}^3, s \in \mathbb{R}, \quad (1)$$

where  $s$  is negative inside the shape and positive outside of it. The iso-surface of (1), *i.e.*, coordinates where it equals 0, corresponds to the shape surface. The insight of deep implicit shapes is that given a set of coordinate/SDF pairs

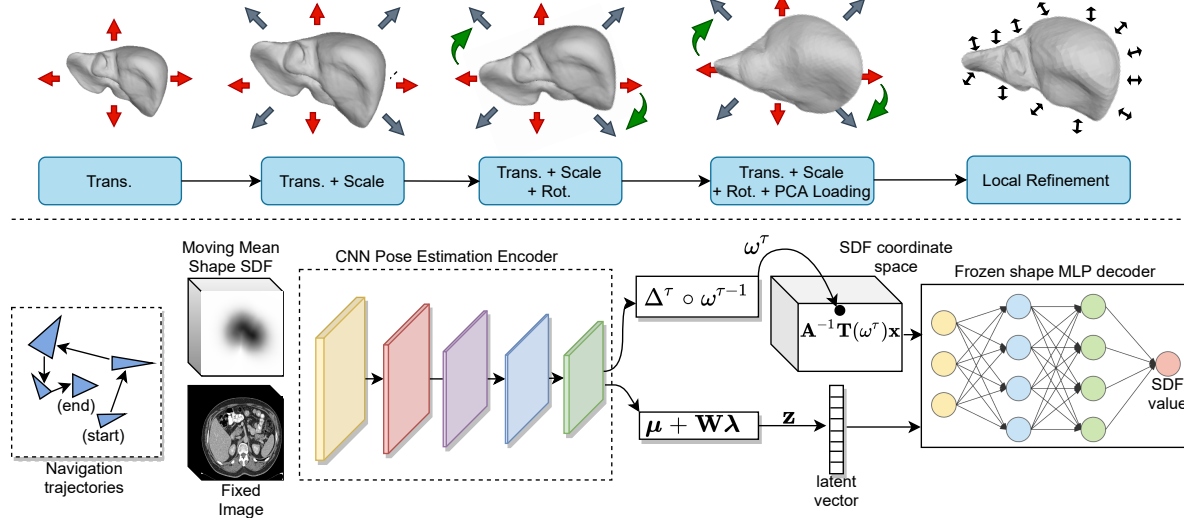


Figure 2. Overview of our deep implicit statistical shape modeling (DISSM) framework.

in some canonical or normalized space,  $\tilde{\mathcal{X}} = \{\tilde{\mathbf{x}}_i, s_i\}$ , a deep MLP can be trained to approximate a shape's SDF:

$$f_{\theta_S}(\tilde{\mathbf{x}}) \approx SDF(\tilde{\mathbf{x}}), \forall \tilde{\mathbf{x}} \in \Omega, \quad (2)$$

where the tilde denotes canonical coordinates. (2) has no resolution limitations as it outputs continuous and smoothly varying values, and, unlike meshes, it does not rely on an explicit discretization scheme. In practice the details actually captured will be governed by the model capacity and the set of samples within  $\mathcal{X}_i$ . While (2) may describe a single shape, it would not describe the anatomical variation across a set of shapes. To do this, we follow Park *et al.*'s powerful and elegant approach of using auto-decoded latent variables [37]. We assume we are given a set of  $K$  SDF samples from the same organ,  $\mathcal{S} = \{\tilde{\mathcal{X}}_k\}_{k=1}^K$ , and we create a corresponding set of latent vectors,  $\mathcal{Z} = \{\mathbf{z}_k\}_{k=1}^K$ . The deep MLP is modified to accept two inputs,  $f_{\theta_S}(\tilde{\mathbf{x}}, \mathbf{z}_k)$ , with the idea being that the output is conditioned by the latent vector to specify which particular SDF is being approximated. We jointly optimize the network weights  $\theta_S$  and latent vectors  $\mathcal{Z}$  to produce the best SDF approximations:

$$\arg \min_{\theta_S, \mathcal{Z}} \sum_k^K \left( \sum_{i=1}^{|\tilde{\mathcal{X}}_k|} \mathcal{L}(f_{\theta_S}(\tilde{\mathbf{x}}_i, \mathbf{z}_k), s_i) + \frac{1}{\sigma^2} \|\mathbf{z}_k\|_2^2 \right), \quad (3)$$

where  $\mathcal{L}$  is the L1 loss and the second term is a zero-mean Gaussian prior whose compactness is controlled by  $\sigma^2$  [37].

The implicit shape model assumes shapes are specified in a canonical space. However, segmentation labels are usually 3D masks in pixel or world coordinates. To create canonical coordinate/SDF training pairs, we first perform within-slice interpolation [1, 55] on masks to remove

the most egregious of discretization artifacts. We then convert the masks to meshes using marching cubes [23], followed by a simplification algorithm [10]. Each mesh is then rigidly aligned to an arbitrarily chosen anchor mesh using coherent point drift [35, 18]. Similar to Park *et al.* [37], SDF and coordinate values are randomly sampled from the mesh, with regions near the surface much more densely sampled. SDF values are also scaled to fit within  $[-1, 1]$ . Based on the anchor mesh, an affine matrix that maps between canonical and pixel coordinates can be constructed,  $\mathbf{x} = \mathbf{A}\tilde{\mathbf{x}}$ .

Once the shape decoder is trained, any latent vector can be inputted into  $f_{\theta_S}(\cdot, \cdot)$  along with a set of coordinates to rasterize an SDF, which can then be rendered and visualized by extracting the iso-boundary. As the top row of Fig. 3 and bottom panel of Fig. 1 demonstrate, the latent space provides a rich description of shape variations. For instance, the mean latent vector,  $\mu$ , produces an anatomically valid shape. A PCA can also capture meaningful variation, *e.g.*, the first basis seems to correspond to stretching and flattening while the second seems to affect the prominence of lobe protuberances. Additionally, interpolating between latent vectors produces reasonable shapes (bottom row of Fig. 3).

### 3.2. Pose Estimation

We now address how to use the compact, rich, and anatomically plausible deep implicit shape space to delineate an object boundary given an image,  $I$ . We need to define: 1) the rigid-body transformation from the canonical coordinates to the image space, and 2) the latent vector that specifies the shape variation. We denote the rigid-body transformation as  $\mathbf{T}(\omega)$  with parameters  $\omega = \{\mathbf{t}, \mathbf{s}, \mathbf{b}\}$ , *i.e.*, translation, anisotropic scale, and rotation, respectively, where  $\mathbf{t} \in \mathbb{R}^3$ ,  $\mathbf{s} \in \mathbb{R}^3$ , and  $\mathbf{b} \in \mathbb{R}^6$ . Here we use Zhou

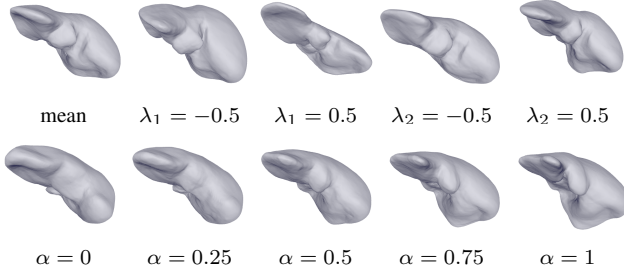


Figure 3. Shape variations captured by the DISSM embedding space constructed using the MSD liver dataset [44]. The top row shows the shapes corresponding to the mean latent vector and the first two PCA basis vectors with negative and positive scales ( $\lambda_1$  and  $\lambda_2$ ). The bottom row renders using the interpolation between two selected latent vectors:  $\mathbf{z} = (1 - \alpha)\mathbf{z}_0 + \alpha\mathbf{z}_1$ .

et al.’s [54] recent six-dimensional parameterization of the rotation matrix, where we actually predict deviations from identity, *i.e.*,  $\mathbf{I} + \mathbf{T}(\mathbf{b})$ . Like most SSMs, we model shape variation using a truncated PCA basis that only captures salient variations:  $\mathbf{z} = \boldsymbol{\mu} + \mathbf{W}\boldsymbol{\lambda}$ . Unlike explicit SSMs [14], the PCA is performed on the latent space and does not require correspondences. We employ an encoder network,  $g_{\theta_E}(I)$ , to predict the rigid pose parameters,  $\omega$ , and the non-rigid PCA loadings  $\boldsymbol{\lambda}$ . Once both the encoder  $g_{\theta_E}(\cdot)$  and the decoder  $f_{\theta_S}(\cdot, \cdot)$  are trained the parameters predicted by  $g_{\theta_E}(\cdot)$  are fed into  $f_{\theta_S}(\cdot, \cdot)$  to produce the object’s SDF:

$$SDF(\mathbf{x}) = f_{\theta_S}(\mathbf{A}^{-1}\mathbf{T}(\omega)\mathbf{x}, \boldsymbol{\mu} + \mathbf{W}\boldsymbol{\lambda}), \quad (4)$$

$$\omega, \boldsymbol{\lambda} = g_{\theta_E}(I), \quad (5)$$

where  $\mathbf{x}$  are coordinates in image space.

Instead of directly predicting pose parameters using (5), we interpret the encoder  $g_{\theta_E}(\cdot)$  as an “agent” that, given an initial pose,  $\omega^0$ , must generate samples along a trajectory by predicting corrections to the previous pose:

$$\Delta^\tau, \boldsymbol{\lambda}^\tau = g_{\theta_E}(I_k, \omega^{\tau-1}), \quad (6)$$

$$\omega^\tau = \Delta^\tau \circ \omega^{\tau-1}, \quad \text{if } \tau > 0, \quad (7)$$

where  $\circ$  denotes the composition of two rigid-body transformations and  $\tau$  indicates the current step in the trajectory. An observation of  $\omega^{\tau-1}$  is injected into the input of the encoder because the encoder needs to be aware of the previous pose to predict the correction. To do this we rasterize the SDF corresponding to the mean shape,  $SDF_{\boldsymbol{\mu}}$ , *once*. After every step it is rigidly transformed using  $\omega^{\tau-1}$  and fed as a second input channel into  $g_{\theta_E}(\cdot, \cdot)$ . The agent-based formulation turns the challenging one-step pose estimation task into a simpler multi-step correction task. Note in (6) we do not predict a trajectory for the PCA loadings. Unlike rigid pose estimation, which can use the transformed  $SDF_{\boldsymbol{\mu}}$ , it is not clear how to best inject a concept of PCA state

into the encoder without rasterizing a new SDF after every step. Since this is prohibitively expensive, the PCA loadings are directly estimated at each step. We break the search space down even further by first predicting rigid poses then predicting the PCA loadings, as detailed below.

### 3.2.1 Rigid Pose Estimation

We first train the encoder  $g_{\theta_E}(\cdot, \cdot)$  to predict rigid poses and we assume a dataset of labelled images is available, allowing for the generation of coordinate/SDF pairs:  $\mathcal{D} = \{I_k, \mathcal{X}_k\}_{k=1}^{K_D}$ , where  $\mathcal{X}_k = \{\mathbf{x}_i, s_i\}$ . Similar to DRL registration approaches [25, 21, 27], in training we generate samples along a trajectory of  $T$  steps, which is referred to as an episode. The encoder is trained by minimizing a loss calculated over the episodes generated on the training data:

$$\arg \min_{\theta_E} \sum_{k=1}^{K_D} \sum_{i=1}^{|\mathcal{X}_k|} \sum_{\tau=1}^T \mathcal{L}(f_{\theta}(\mathbf{A}^{-1}\mathbf{T}(\omega^\tau)\mathbf{x}_i, \boldsymbol{\mu}), s_i), \quad (8)$$

where back-propagation is only executed on the encoder weights  $\theta_E$  within each step  $\tau$ , and the dependence on  $g_{\theta_E}(\cdot)$  is implied through  $\omega_\tau$ . Note that (8) uses the mean latent vector,  $\boldsymbol{\mu}$ , to generate SDF predictions and the  $\boldsymbol{\lambda}$  output in (6) is ignored for now. This training process shares similarities to DRL, particularly in its formulation of the prediction step as an MDP. Unlike DRL, and similar to MDP registration tasks [25, 21, 27], there is no need for using cumulative rewards because a meaningful loss can be directly calculated. At the start of training, the agent will not produce reliable trajectories but, as the model strengthens, the playing out of an *episode* of  $T$  steps for each training iteration will better sample meaningful states for the agent to learn from. To expose the agent to a greater set of states, we also inject random pose perturbations,  $\eta$ , after every step, modifying (6) and (7) to

$$\Delta^\tau, \boldsymbol{\lambda}^\tau = g_{\theta_E}(I_k, \eta^\tau \circ \omega^{\tau-1}), \quad (9)$$

$$\omega^\tau = \Delta^\tau \circ \eta^\tau \circ \omega^{\tau-1}, \quad \text{if } \tau > 0. \quad (10)$$

A downside to the episodic training is that each image is sampled consecutively  $T$  times, which can introduce instability and overfitting to the learning process. To address this we introduce *inverted episodic training*, altering the loop order to make each episodic step play out as an outer loop:

$$\arg \min_{\theta_E} \sum_{\tau=1}^T \sum_{k=1}^{K_D} \sum_{i=1}^{|\mathcal{X}_k|} \mathcal{L}(f_{\theta}(\mathbf{A}^{-1}\mathbf{T}(\omega^\tau)\mathbf{x}_i, \boldsymbol{\mu}), s_i), \quad (11)$$

which requires saving  $\omega^\tau$  for each sample after each iteration. Although mechanistically very different, inverted episodic training shares a similar purpose as memory replay in DRL [34], *i.e.*, better sample meaningful states that the agent is likely to encounter in inference.

Stage	$\Delta$	$\eta$	$\omega^0$
Trans.	$\mathbf{t}$	$\eta_t$	$\omega_{\mathcal{D}}$
Scale	$\{\mathbf{s}, \mathbf{t}\}$	$\eta_s \circ \eta'_t$	$\{\omega_{t,k}^T\}_{k=1}^{K_{\mathcal{D}}}$
Rot.	$\{\mathbf{b}, \mathbf{s}, \mathbf{t}\}$	$\eta_r \circ \eta'_s \circ \eta'_t$	$\{\omega_{s,k}^T\}_{k=1}^{K_{\mathcal{D}}}$
Non Rig.	$\{\mathbf{b}, \mathbf{s}, \mathbf{t}\}$	$\eta'_r \circ \eta'_s \circ \eta'_t$	$\{\omega_{r,k}^T\}_{k=1}^{K_{\mathcal{D}}}$

Table 1. Marginal space learning (MSL) schedule used in DISSM.

**Marginal Space Learning:** While the MDP of (11) provides a meaningful sampling strategy, it still requires searching amongst all possible translation, scale, and rotation options, which is too complex and large. Indeed in our experiments we were unable to ever reliably produce trajectories that converged. To solve this, DISSMs adopt marginal space learning (MSL) [52, 51], designed to deal with this very problem. In short, MSL decomposes the search process into a chain of dependant estimates, focusing on one set while marginalizing or integrating out the others. As Tab. 1 outlines, in practice this means that we first limit the search space by training the encoder to only predict a translation trajectory,  $\mathbf{t}$ , with the random perturbations also limited to only translation, *i.e.*,  $\eta_t$ . The initial pose for all samples is the mean location in the training set, denoted  $\omega_{\mathcal{D}}$ . Once trained, the translation encoder weights and final poses,  $\{\omega_{t,k}^T\}_{k=1}^{K_{\mathcal{D}}}$ , are used to initialize a scale encoder of identical architecture, but one that predicts scale corrections,  $\mathbf{s}$ , in addition to finetuning the translation. Importantly, to focus the search space on scale, the random translation perturbations are configured to be much smaller than before, which is represented by the prime modifier on  $\eta'_t$ . Finally, a rotation model is trained (while finetuning translation + scale). In inference, the rigid pose is estimated by successively applying the models of each stage, using the final pose of the previous step to initialize the next.

### 3.2.2 Non-Rigid Pose Estimation

Once a rigid pose estimated, anatomically plausible deformations can then be estimated. We initialize the weights and poses of the non-rigid encoder using the translation + scale + rotation rigid model, modifying (11) to now incorporate the PCA basis:

$$\arg \min_{\theta_E} \sum_{\tau=1}^T \sum_{k=1}^{K_{\mathcal{D}}} \sum_{i=1}^{|\mathcal{X}_k|} \mathcal{L}(f_{\theta}(\mathbf{A}^{-1} \mathbf{T}(\omega_{\tau}) \mathbf{x}_i, \boldsymbol{\mu} + \mathbf{W} \boldsymbol{\lambda}^{\tau}), s_i) + \frac{1}{\sigma^2} \|\boldsymbol{\mu} + \mathbf{W} \boldsymbol{\lambda}^{\tau}\|_2^2 \quad (12)$$

As Table 1 indicates, the random rigid perturbations are configured to be small in magnitude to confine the search space to primarily the PCA loadings.

### 3.3. Surface Refinement

Like classic SSMs [14], non-rigid pose estimation provides a robust and anatomically plausible prediction, but it may fail to capture very fine details. We execute local refinements using an FCN model,  $r = h_{\theta_R}(I, SDF_{\lambda})$ , that accepts a two-channel input comprising the 3D image and the rasterized SDF after the non-rigid shape estimation. Its goal is to refine the  $SDF_{\lambda}$  to better match the ground truth SDF. To retain an implicit surface representation, we adapt portions of a recent deep level set loss [31]:

$$\begin{aligned} \mathcal{L}_r = & \sum_{\mathbf{x} \in \Omega_b} (SDF(\mathbf{x})^2 \cdot \delta_{\epsilon}(SDF_{\lambda}(\mathbf{x}) + r(\mathbf{x})))^{1/2} \\ & + \lambda_1 \sum_{\mathbf{x} \in \Omega_b} (\|\nabla(SDF_{\lambda}(\mathbf{x}) + r(\mathbf{x}))\| - 1)^2 \\ & + \lambda_2 \sum_{\mathbf{x} \in \Omega_b} |\max(0, r(\mathbf{x}) - \rho)|, \end{aligned} \quad (13)$$

where  $SDF$  is the ground truth SDF and  $\delta_{\epsilon}$  is a differentiable approximation of the Dirac-delta function. The first term ensures the iso-boundary of the refined SDF matches the ground-truth iso-boundary, whereas the second term ensures a unit gradient everywhere, guaranteeing that it remains a proper SDF. See Michalkiewicz *et al.* [31] for more details. We add the third term to ensure the refinement does not deviate too much from  $SDF_{\lambda}$  beyond a margin,  $\rho$ , otherwise the refinement is free to deviate from  $SDF_{\lambda}$  without penalty. Following standard level set practices, we only produce refinements within a narrow band,  $\Omega_b$ , around the  $SDF_{\lambda}$  iso-boundary, which is also represented in the loss of (13). Finally, in addition to standard data augmentations to  $I$ , we also independently augment  $SDF_{\lambda}$  with random rigid and non-rigid pose variations, enriching the model’s training set.

## 4. Experiments

**Datasets:** We evaluate DISSM on delineating pathological livers from venous-phase CTs. We use the size-131 training set of the MSD liver dataset [44], splitting it randomly into training, testing, and validation using proportions of 70%, 20%, and 10%, respectively. Tumor masks were merged into the liver to create a pathological liver mask. To measure how well DISSM operates in clinical deployments, we also investigate how well the MSD-trained DISSM can perform on an external and independent *clinical* dataset [39]. We use only the test set of Raju *et al.* [39], which comprises 97 venous-phase CTs. No patient studies from this dataset were involved in our training process. Collected directly from hospital archives with minimal curation, the dataset includes challenging scenarios not seen in the MSD dataset, *i.e.*, intrahepatic cholangiocellular carcinoma (ICC), benign lesions, and transarterial

chemoembolization (TACE)-treated hepatocellular carcinomas (HCCs). Additionally, other morbidities are highly represented, such as liver fibrosis and splenomegaly [39] and demographics are different (Asian population vs. mostly Western population in MSD [44]). Thus, the dataset helps reveal whether the DISSM anatomical priors can provide robustness against unforeseeable and challenging clinical scenarios not represented in a training set.

**Implementation Details:** To train the shape decoder,  $f_{\theta_S}(\cdot, \cdot)$ , we extract coordinate/SDF pairs from the masks using the procedure outlined in Sec. 3.1. The shape decoder structure and hyperparameters follow that of Park *et al.* [37] and we use a size 256 latent variable. For the pose encoder,  $g_{\theta_E}(\cdot, \cdot)$ , we downsample all 3D volumes to a  $4 \times 4 \times 4$ mm resolution and use the 3D encoder of a 3D U-Net [6], with 4 downsampling layers and global averaging pooling to produce  $\Delta^\tau$  and  $\Lambda$ . We only estimate the first 28 PCA components, which correspond to 72% of the variance. The number of inverted episodic steps,  $T$ , for training the translation, scale, rotation, and non-rigid encoders was 7, 15, 15, and 15, respectively. After the translation encoder converged, volumes were cropped to a  $128 \times 108 \times 88$  area to eliminate irrelevant image regions from the field of view for subsequent steps. Finally, we use a 3D U-Net [6] as the local surface refinement model,  $h_{\theta_R}(\cdot, \cdot)$ , and train it on full resolution volumes. Full training details, including the schedule of random pose perturbations and a complete listing of all hyperparameters, can be found in the supplementary.

**Experimental Setup:** We compare DISSM against some of the strongest FCN alternatives we are aware of. 1) nnU-Net [16], the winner of the MSD [44] and KiTS [15] challenges. We use its dual model 3D cascade setting, which performed best on the liver portion of the MSD challenge. 2) HDenseUNet [24], a leader of the LiTS challenge [3] that uses a cascade of 2D and 3D FCNs. 3) 2D P-HNN [13], used as an FCN backbone for a recent semi-supervised liver segmentation method [39]. For all, we use their published implementations, including recommended resolutions, pre- and post-processing, and data augmentations. To compare against these models, we threshold the DISSM SDFs to create a mask and measure the DSC, average symmetric surface distance (ASSD), and HD scores against the original masks. *Note, this is a disadvantageous setup for DISSM, as the original masks suffer from stair-like discretization effects, which DISSM aims to rectify.*

**Results:** DISSM consumes 12 – 13s to fully delineate a 3D volume. Fig. 4 overlays the DISSM results on top of a CT scan after each stage. As can be seen, each stage progressively improves the result. After the non-rigid PCA loading, the delineation quality is already quite high, capturing a lobe curve not represented by the mean shape. The local refinement improves results even further by capturing fine-grained boundary curvatures.

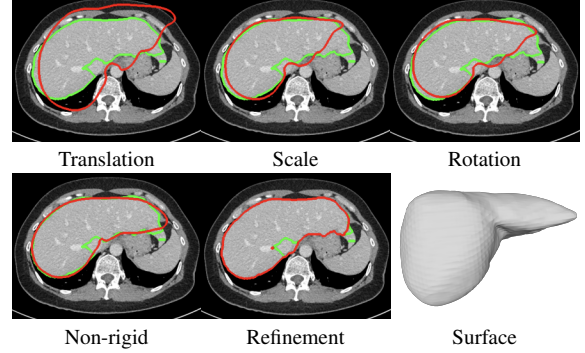


Figure 4. Illustration of the pose estimation process of DISSM. Red and green contours represent the current estimate and the ground truth of liver delineations, respectively.

Model	DSC (%)	ASSD (mm)	HD (mm)
2D-PHNN	$95.9 \pm 2.7$	$2.6 \pm 1.2$	$35.7 \pm 16.1$
nnU-Net (cascade)	$96.4 \pm 1.9$	$1.7 \pm 0.9$	$29.1 \pm 12.4$
H-DenseUNet	$96.3 \pm 2.1$	$1.9 \pm 1.1$	$30.4 \pm 13.9$
DISSM w/o refine	$96.1 \pm 0.9$	$1.5 \pm 0.7$	$23.4 \pm 12.2$
DISSM w refine	<b><math>96.5 \pm 0.7</math></b>	<b><math>1.1 \pm 0.7</math></b>	<b><math>21.4 \pm 11.8</math></b>

Table 2. Quantitative results on the MSD liver dataset [44].

Model	DSC (%)	ASSD (mm)	HD (mm)
2D-PHNN	$90.1 \pm 5.1$	$3.9 \pm 1.4$	$46.3 \pm 21.1$
nnU-Net (cascade)	$92.4 \pm 3.3$	$3.6 \pm 1.1$	$34.1 \pm 17.3$
HDenseUNet	$92.1 \pm 3.7$	$3.3 \pm 1.3$	$36.2 \pm 16.7$
DISSM w/o refine	$95.7 \pm 1.8$	$2.6 \pm 1.1$	$24.7 \pm 12.6$
DISSM w refine	<b><math>95.9 \pm 1.6</math></b>	<b><math>2.3 \pm 0.9</math></b>	<b><math>21.8 \pm 12.1</math></b>

Table 3. Cross-dataset results on the clinical liver dataset [39].

Table 2 outlines the performance on the MSD data. As can be seen, all models perform quite well. When local refinement is added to DISSM, it posts slightly better mean DSC values and more significantly better ASSD scores than alternatives. More importantly, DISSM exhibits much less variability in DSC and ASSD scores than competitors, indicating better robustness. This is cogently illustrated by the HD numbers, *i.e.*, the worst-case distances for each volume. DISSM dramatically improves the HD numbers by roughly 26% to 40%, corresponding to much more reliable delineations. These improvements in robustness are further illustrated by the box and whisker DSC plot of Fig. 5, which shows DISSM posting better worst case performances (96.0% vs 95.1% compared to the best alternative of nnU-Net). Third quartile values are also noticeably improved. The visual impact of these improvements can be seen in the first row of Fig. 4 where DISSM avoids some highly detrimental leakages into the stomach.

While the above demonstrate that DISSM can provide superior intra-dataset performance, the cross-dataset clini-

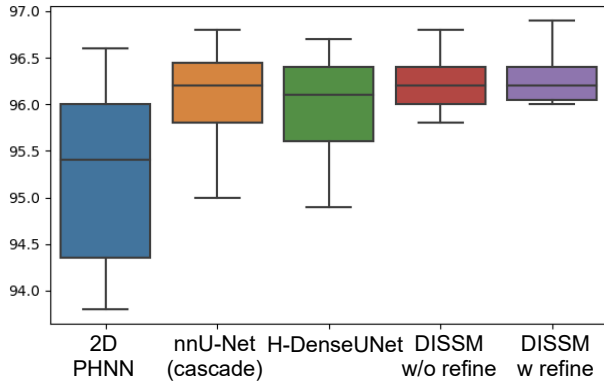


Figure 5. Box and whisker plot of DSC scores on the MSD liver dataset [44].

cal results are even more telling. As Table 3 highlights, the competitor model performances drop drastically on the clinical dataset, underscoring the difficulty of operating when morbidities, scanners, patient populations, and practices can vary in unanticipated ways. The second to fourth rows of Fig. 4 illustrate challenging examples of the dataset, where the competitor methods leaked into the cardiac region, failed to segment a TACE lesion, and failed to handle a patient with splenomegaly. Note, the fourth row represents the worst-case result for DISSM. In contrast, DISSM’s performance is much more stable, still posting very good numbers. Compared to the competitors, DISSM boosts the mean DSC score by 3.5 to 5.8% and reduces the HD by 36 to 53%. The box and whisker plot of Fig. 7 provides further insight into the differences in robustness. The best fully-supervised competitor, *i.e.*, nnU-Net posts a worst-case DSC performance of 88.1%, whereas DISSM’s worst-case performance is a much better 93.2%. Moreover, the spread in results, *e.g.*, the quartiles, are considerably smaller. Given that clinical deployments are the ultimate end goal of delineation solutions, these results offer convincing demonstration of the benefits of imposing strong and descriptive anatomical priors for segmentation.

## 5. Conclusion

We present deep implicit statistical shape models (DISSMs), a novel delineation approach that uses 1) a deep implicit model to construct statistical and correspondence-free anatomical priors, and 2) directly outputs high-quality surfaces, rather than voxelized masks. To fit a shape to a new image, DISSM uses a novel and robust pose estimation procedure that incorporates MSL and inverted episodic training. As such, we are the first to integrate a true SSM with deep learning technology. Cross dataset evaluations on pathological liver segmentation demonstrate that DISSM can outperform arguably the leading FCN today

(nnU-Net [16]), reducing the mean HD by 12.3mm, and improving the mean and worst-case DSC by 3.5% and 5.1%, respectively. While continued maturation is necessary, DISSM represents a new and promising approach to 3D medical imaging delineation.

## References

- [1] A. B. Albu, T. Beugeling, and D. Laurendeau. A morphology-based approach for interslice interpolation of anatomical slices from volumetric images. *IEEE Transactions on Biomedical Engineering*, 55(8):2022–2038, 2008. 4, 12
- [2] Riddhish Bhalodia, Shireen Y. Elhabian, Ladislav Kavan, and Ross T. Whitaker. DeepSSM: A Deep Learning Framework for Statistical Shape Modeling from Raw Images. In Martin Reuter, Christian Wachinger, Hervé Lombaert, Beatriz Paniagua, Marcel Lüthi, and Bernhard Egger, editors, *Shape in Medical Imaging*, Lecture Notes in Computer Science, pages 244–257, Cham, 2018. Springer International Publishing. 2, 3
- [3] Patrick Bilic, Patrick Ferdinand Christ, Eugene Vorontsov, Grzegorz Chlebus, Hao Chen, Qi Dou, Chi-Wing Fu, Xiao Han, Pheng-Ann Heng, Jürgen Hesser, Samuel Kadoury, Tomasz K. Konopczynski, Miao Le, Chunming Li, Xiaomeng Li, Jana Lipková, John S. Lowengrub, Hans Meine, Jan Hendrik Moltz, Chris Pal, Marie Piraud, Xiaojuan Qi, Jin Qi, Markus Rempfler, Karsten Roth, Andrea Schenck, Anjany Sekuboyina, Ping Zhou, Christian Hüsemeyer, Marcel Beetz, Florian Ettlinger, Felix Grün, Georgios Kaassis, Fabian Lohöfer, Rickmer Braren, Julian Holch, Felix Hofmann, Wieland H. Sommer, Volker Heinemann, Colin Jacobs, Gabriel Efrain Humpire Mamani, Bram van Ginneken, Gabriel Chartrand, An Tang, Michal Drozdza, Avi Ben-Cohen, Eyal Klang, Michal Marianne Amitai, Eli Konnen, Hayit Greenspan, Johan Moreau, Alexandre Hostettler, Luc Soler, Rafael Vivanti, Adi Szeskin, Naama Lev-Cohain, Jacob Sosna, Leo Joskowicz, and Bjoern H. Menze. The liver tumor segmentation benchmark (lits). *CoRR*, abs/1901.04056, 2019. 7
- [4] Jinzheng Cai, Yingda Xia, Dong Yang, Daguang Xu, Lin Yang, and Holger Roth. End-to-End Adversarial Shape Learning for Abdomen Organ Deep Segmentation. In Heung-Il Suk, Mingxia Liu, Pingkun Yan, and Chunfeng Lian, editors, *Machine Learning in Medical Imaging*, Lecture Notes in Computer Science, pages 124–132, Cham, 2019. Springer International Publishing. 2, 3
- [5] Zhiqin Chen and Hao Zhang. Learning Implicit Fields for Generative Shape Modeling. In *2019 IEEE/CVF Conference on Computer Vision and Pattern Recognition (CVPR)*, pages 5932–5941, Long Beach, CA, USA, June 2019. IEEE. 2, 3
- [6] Özgün Çiçek, Ahmed Abdulkadir, Soeren S. Lienkamp, Thomas Brox, and Olaf Ronneberger. 3d u-net: Learning dense volumetric segmentation from sparse annotation. In Sébastien Ourselin, Leo Joskowicz, Mert R. Sabuncu, Gozde Unal, and William Wells, editors, *Medical Image Computing and Computer-Assisted Intervention – MICCAI 2016*, pages 424–432, Cham, 2016. Springer International Publishing. 7

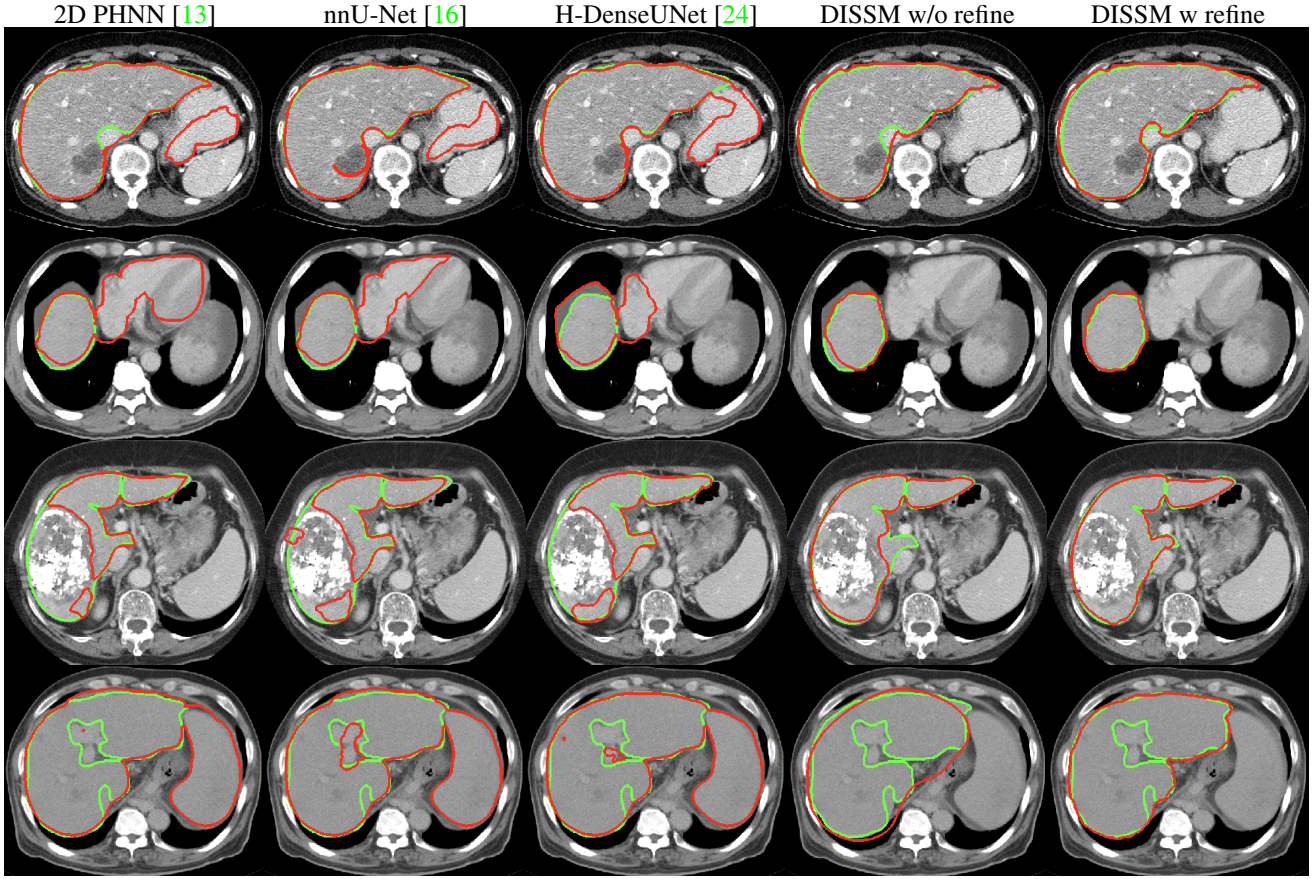


Figure 6. Qualitative comparison of DISSM (without or with refinement) versus three state-of-the-art competitor approaches [13, 16, 24]. Red and green contours represent the current estimate and the ground truth of liver delineations, respectively. The first and second-to-fourth rows are drawn from the MSD and clinical dataset, respectively. Fourth row is worst-case performance for DISSM.

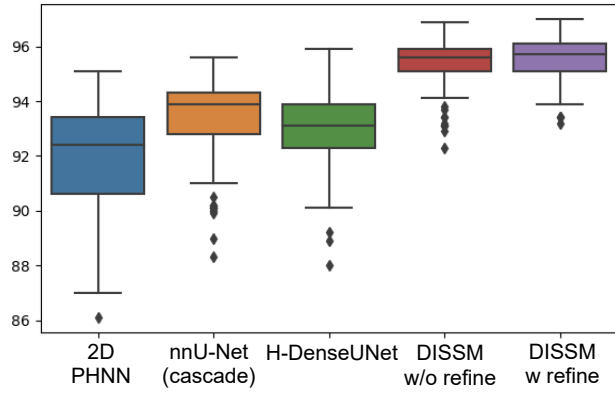


Figure 7. Box-whisker plot of DSC scores on the clinical dataset.

[7] Özgün Çiçek, Ahmed Abdulkadir, Soeren S Lienkamp, Thomas Brox, and Olaf Ronneberger. 3d u-net: learning dense volumetric segmentation from sparse annotation. In *International conference on medical image computing and computer-assisted intervention*, pages 424–432. Springer,

2016. 14

[8] T. F. Cootes, C. J. Taylor, D. H. Cooper, and J. Graham. Training models of shape from sets of examples. In David Hogg and Roger Boyle, editors, *BMVC92*, pages 9–18, London, 1992. Springer London. 2, 3

[9] Daniel Cremers, Mikael Rousson, and Rachid Deriche. A Review of Statistical Approaches to Level Set Segmentation: Integrating Color, Texture, Motion and Shape. *International Journal of Computer Vision*, 72(2):195–215, Apr. 2007. 3

[10] Sven Forstmann. Fast-quadruc-mesh-simplification. <https://github.com/sp4cerat/Fast-Quadruc-Mesh-Simplification>, 2020. 4, 12

[11] Romane Gauriau, Rémi Cuingnet, David Lesage, and Isabelle Bloch. Multi-organ localization with cascaded global-to-local regression and shape prior. *Medical image analysis*, 23(1):70–83, 2015. 3

[12] Florin-Cristian Ghesu, Bogdan Georgescu, Yefeng Zheng, Sasa Grbic, Andreas Maier, Joachim Hornegger, and Dorin Comaniciu. Multi-scale deep reinforcement learning for real-time 3d-landmark detection in ct scans. *IEEE transactions on pattern analysis and machine intelligence*, 41(1):176–189, 2017. 3

[13] Adam P. Harrison, Ziyue Xu, Kevin George, Le Lu, Ronald M. Summers, and Daniel J. Mollura. Progressive and multi-path holistically nested neural networks for pathological lung segmentation from ct images. In Maxime Descoteaux, Lena Maier-Hein, Alfred Franz, Pierre Jannin, D. Louis Collins, and Simon Duchesne, editors, *Medical Image Computing and Computer Assisted Intervention – MICCAI 2017*, pages 621–629, Cham, 2017. Springer International Publishing. [2](#), [7](#), [9](#)

[14] Tobias Heimann and Hans-Peter Meinzer. Statistical shape models for 3d medical image segmentation: A review. *Medical Image Analysis*, 13(4):543–563, 2009. [2](#), [3](#), [5](#), [6](#)

[15] Nicholas Heller, Fabian Isensee, Klaus H Maier-Hein, Xiaoshuai Hou, Chunmei Xie, Fengyi Li, Yang Nan, Guangrui Mu, Zhiyong Lin, Miofie Han, et al. The state of the art in kidney and kidney tumor segmentation in contrast-enhanced ct imaging: Results of the kits19 challenge. *Medical Image Analysis*, page 101821, 2020. [7](#)

[16] Fabian Isensee, Paul F. Jaeger, Simon A. A. Kohl, Jens Petersen, and Klaus H. Maier-Hein. nnU-Net: a self-configuring method for deep learning-based biomedical image segmentation. *Nature Methods*, 18(2):203–211, Feb. 2021. Number: 2 Publisher: Nature Publishing Group. [1](#), [2](#), [7](#), [8](#), [9](#)

[17] Fabian Isensee, Jens Petersen, Andre Klein, David Ziemmerer, Paul F Jaeger, Simon Kohl, Jakob Wasserthal, Gregor Koehler, Tobias Norajitra, Sebastian Wirkert, et al. nnu-net: Self-adapting framework for u-net-based medical image segmentation. *arXiv preprint arXiv:1809.10486*, 2018. [3](#), [14](#)

[18] Siavash Khallaghi. Pycpd. <https://github.com/siavashk/pycpd>, 2020. [4](#), [12](#)

[19] Diederik P. Kingma and Jimmy Ba. Adam: A method for stochastic optimization. In Yoshua Bengio and Yann LeCun, editors, *3rd International Conference on Learning Representations, ICLR 2015, San Diego, CA, USA, May 7-9, 2015, Conference Track Proceedings*, 2015. [12](#)

[20] Marian Kleineberg. mesh-to-sdf. [https://github.com/marian42/mesh\\_to\\_sdf](https://github.com/marian42/mesh_to_sdf), 2020. [12](#)

[21] Julian Krebs, Tommaso Mansi, Hervé Delingette, Li Zhang, Florin C Ghesu, Shun Miao, Andreas K Maier, Nicholas Ayache, Rui Liao, and Ali Kamen. Robust non-rigid registration through agent-based action learning. In *International Conference on Medical Image Computing and Computer-Assisted Intervention*, pages 344–352. Springer, 2017. [3](#), [5](#)

[22] Kisuk Lee, Jonathan Zung, Peter Li, Viren Jain, and H Sebastian Seung. Superhuman accuracy on the snemi3d connectomics challenge. *arXiv preprint arXiv:1706.00120*, 2017. [12](#)

[23] Thomas Lewiner, Hélio Lopes, Antônio Wilson Vieira, and Geovan Tavares. Efficient implementation of marching cubes’ cases with topological guarantees. *Journal of Graphics Tools*, 8(2):1–15, 2003. [4](#), [12](#)

[24] X. Li, H. Chen, X. Qi, Q. Dou, C. W. Fu, and P. A. Heng. H-denseunet: Hybrid densely connected unet for liver and tumor segmentation from ct volumes. *IEEE Transactions on Medical Imaging*, 37(12):2663–2674, 2018. [2](#), [7](#), [9](#), [14](#)

[25] Rui Liao, Shun Miao, Pierre de Tournemire, Sasa Grbic, Ali Kamen, Tommaso Mansi, and Dorin Comaniciu. An artificial agent for robust image registration. In *Proceedings of the AAAI Conference on Artificial Intelligence*, volume 31, 2017. [3](#), [5](#)

[26] Jonathan Long, Evan Shelhamer, and Trevor Darrell. Fully convolutional networks for semantic segmentation. In *Proceedings of the IEEE Conference on Computer Vision and Pattern Recognition (CVPR)*, June 2015. [1](#)

[27] Kai Ma, Jiangping Wang, Vivek Singh, Birgi Tumeroy, Yao-Jen Chang, Andreas Wimmer, and Terrence Chen. Multi-modal image registration with deep context reinforcement learning. In *International Conference on Medical Image Computing and Computer-Assisted Intervention*, pages 240–248. Springer, 2017. [3](#), [5](#)

[28] C. R. Maurer, Rensheng Qi, and V. Raghavan. A linear time algorithm for computing exact euclidean distance transforms of binary images in arbitrary dimensions. *IEEE Transactions on Pattern Analysis and Machine Intelligence*, 25(2):265–270, 2003. [12](#)

[29] Matthew Michael McCormick, Xiaoxiao Liu, Luis Ibanez, Julien Jomier, and Charles Marion. Itk: enabling reproducible research and open science. *Frontiers in neuroinformatics*, 8:13, 2014. [13](#)

[30] Lars Mescheder, Michael Oechsle, Michael Niemeyer, Sebastian Nowozin, and Andreas Geiger. Occupancy Networks: Learning 3D Reconstruction in Function Space. In *2019 IEEE/CVF Conference on Computer Vision and Pattern Recognition (CVPR)*, pages 4455–4465, Long Beach, CA, USA, June 2019. IEEE. [2](#), [3](#)

[31] Mateusz Michalkiewicz, Jhony Kaesemel Pontes, Dominic Jack, Mahsa Baktashmotagh, and Anders Eriksson. Implicit Surface Representations As Layers in Neural Networks. In *2019 IEEE/CVF International Conference on Computer Vision (ICCV)*, pages 4742–4751, Seoul, Korea (South), Oct. 2019. IEEE. [2](#), [3](#), [6](#)

[32] Fausto Milletari, Nassir Navab, and Seyed-Ahmad Ahmadi. V-net: Fully convolutional neural networks for volumetric medical image segmentation. In *2016 fourth international conference on 3D vision (3DV)*, pages 565–571. IEEE, 2016. [3](#)

[33] Fausto Milletari, Alex Rothberg, Jimmy Jia, and Michal Sofka. Integrating Statistical Prior Knowledge into Convolutional Neural Networks. In Maxime Descoteaux, Lena Maier-Hein, Alfred Franz, Pierre Jannin, D. Louis Collins, and Simon Duchesne, editors, *Medical Image Computing and Computer Assisted Intervention – MICCAI 2017*, Lecture Notes in Computer Science, pages 161–168, Cham, 2017. Springer International Publishing. [2](#), [3](#)

[34] Volodymyr Mnih, Koray Kavukcuoglu, David Silver, Andrei A. Rusu, Joel Veness, Marc G. Bellemare, Alex Graves, Martin Riedmiller, Andreas K. Fidjeland, Georg Ostrovski, Stig Petersen, Charles Beattie, Amir Sadik, Ioannis Antonoglou, Helen King, Dharshan Kumaran, Daan Wierstra, Shane Legg, and Demis Hassabis. Human-level control through deep reinforcement learning. *Nature*, 518(7540):529–533, Feb. 2015. Number: 7540 Publisher: Nature Publishing Group. [3](#), [5](#)

[35] A. Myronenko and X. Song. Point set registration: Coherent point drift. *IEEE Transactions on Pattern Analysis and Machine Intelligence*, 32(12):2262–2275, 2010. 4, 12

[36] Ozan Oktay, Enzo Ferrante, Konstantinos Kamnitsas, Matthias Heinrich, Wenjia Bai, Jose Caballero, Ricardo Guerrero, Stuart Cook, Antonio de Marvao, Timothy Dawes, Declan O’Regan, Bernhard Kainz, Ben Glocker, and Daniel Rueckert. Anatomically Constrained Neural Networks (ACNN): Application to Cardiac Image Enhancement and Segmentation. *IEEE Transactions on Medical Imaging*, PP, May 2017. 2, 3

[37] Jeong Joon Park, Peter Florence, Julian Straub, Richard Newcombe, and Steven Lovegrove. Deep sdf: Learning continuous signed distance functions for shape representation. In *Proceedings of the IEEE Conference on Computer Vision and Pattern Recognition*, pages 165–174, 2019. 2, 3, 4, 7, 12

[38] pmneila. Pymcubes. <https://github.com/pmneila/PyMCubes>, 2020. 12

[39] Ashwin Raju, Chi-Tung Cheng, Yuankai Huo, Jinzheng Cai, Junzhou Huang, Jing Xiao, Le Lu, ChienHung Liao, and Adam P. Harrison. Co-heterogeneous and adaptive segmentation from multi-source and multi-phase ct imaging data: A study on pathological liver and lesion segmentation. In Andrea Vedaldi, Horst Bischof, Thomas Brox, and Jan-Michael Frahm, editors, *Computer Vision – ECCV 2020*, pages 448–465, Cham, 2020. Springer International Publishing. 2, 6, 7, 14

[40] Ashwin Raju, Zhanghexuan Ji, Chi Tung Cheng, Jinzheng Cai, Junzhou Huang, Jing Xiao, Le Lu, ChienHung Liao, and Adam P. Harrison. User-Guided Domain Adaptation for Rapid Annotation from User Interactions: A Study on Pathological Liver Segmentation. In Anne L. Martel, Purang Abolmaesumi, Danail Stoyanov, Diana Mateus, Maria A. Zuluaga, S. Kevin Zhou, Daniel Racoceanu, and Leo Joskowicz, editors, *Medical Image Computing and Computer Assisted Intervention – MICCAI 2020*, Lecture Notes in Computer Science, pages 457–467, Cham, 2020. Springer International Publishing. 2, 3

[41] H. Ravishankar, R. Venkataramani, S. Thiruvenkadam, P. Sudhakar, and V. Vaidya. Learning and Incorporating Shape Models for Semantic Segmentation. In Maxime Descoteaux, Lena Maier-Hein, Alfred Franz, Pierre Jannin, D. Louis Collins, and Simon Duchesne, editors, *Medical Image Computing and Computer Assisted Intervention – MICCAI 2017*, Lecture Notes in Computer Science, pages 203–211, Cham, 2017. Springer International Publishing. 2, 3

[42] Tim Salimans and Diederik P. Kingma. Weight normalization: A simple reparameterization to accelerate training of deep neural networks. *CoRR*, abs/1602.07868, 2016. 12

[43] J.A. Sethian. *Level Set Methods and Fast Marching Methods*. Cambridge Press, 1999. 13

[44] Amber L. Simpson, Michela Antonelli, Spyridon Bakas, Michel Bilello, Keyvan Farahani, Bram van Ginneken, Annette Kopp-Schneider, Bennett A. Landman, Geert Litjens, Bjoern H. Menze, Olaf Ronneberger, Ronald M. Summers, Patrick Bilic, Patrick Ferdinand Christ, Richard K. G. Do, Marc Gollub, Jennifer Golia-Pernicka, Stephan Heckers, William R. Jarnagin, Maureen McHugo, Sandy Napel, Eugene Vorontsov, Lena Maier-Hein, and M. Jorge Cardoso. A large annotated medical image dataset for the development and evaluation of segmentation algorithms. *CoRR*, abs/1902.09063, 2019. 1, 2, 5, 6, 7, 8

[45] Darko Štern, Thomas Ebner, and Martin Urschler. From local to global random regression forests: Exploring anatomical landmark localization. In *International Conference on Medical Image Computing and Computer-Assisted Intervention*, pages 221–229. Springer, 2016. 3

[46] Laurens van der Maaten and Geoffrey Hinton. Visualizing data using t-sne. *Journal of Machine Learning Research*, 9(86):2579–2605, 2008. 2

[47] Udaranga Wickramasinghe, Edoardo Remelli, Graham Knott, and Pascal Fua. Voxel2Mesh: 3D Mesh Model Generation from Volumetric Data. In Anne L. Martel, Purang Abolmaesumi, Danail Stoyanov, Diana Mateus, Maria A. Zuluaga, S. Kevin Zhou, Daniel Racoceanu, and Leo Joskowicz, editors, *Medical Image Computing and Computer Assisted Intervention – MICCAI 2020*, Lecture Notes in Computer Science, pages 299–308, Cham, 2020. Springer International Publishing. 3

[48] Qiangeng Xu, Weiyue Wang, Duygu Ceylan, Radomir Mech, and Ulrich Neumann. Disn: Deep implicit surface network for high-quality single-view 3d reconstruction. In *NeurIPS*, 2019. 3

[49] Dong Yang, Daguang Xu, S. Kevin Zhou, Bogdan Georgescu, Mingqing Chen, Sasa Grbic, Dimitris Metaxas, and Dorin Comaniciu. Automatic Liver Segmentation Using an Adversarial Image-to-Image Network. In Maxime Descoteaux, Lena Maier-Hein, Alfred Franz, Pierre Jannin, D. Louis Collins, and Simon Duchesne, editors, *Medical Image Computing and Computer Assisted Intervention – MICCAI 2017*, Lecture Notes in Computer Science, pages 507–515, Cham, 2017. Springer International Publishing. 2, 3

[50] Jiawen Yao, Jinzheng Cai, Dong Yang, Daguang Xu, and Junzhou Huang. Integrating 3D Geometry of Organ for Improving Medical Image Segmentation. In Dinggang Shen, Tianming Liu, Terry M. Peters, Lawrence H. Staib, Caroline Essert, Sean Zhou, Pew-Thian Yap, and Ali Khan, editors, *Medical Image Computing and Computer Assisted Intervention – MICCAI 2019*, Lecture Notes in Computer Science, pages 318–326, Cham, 2019. Springer International Publishing. 3

[51] Y. Zheng, A. Barbu, B. Georgescu, M. Scheuering, and D. Comaniciu. Four-chamber heart modeling and automatic segmentation for 3-d cardiac ct volumes using marginal space learning and steerable features. *IEEE Transactions on Medical Imaging*, 27(11):1668–1681, 2008. 2, 3, 6

[52] Yefeng Zheng and Dorin Comaniciu. *Marginal space learning for medical image analysis*. Springer, 2014. 2, 3, 6

[53] Yefeng Zheng, David Liu, Bogdan Georgescu, Hien Nguyen, and Dorin Comaniciu. 3d deep learning for efficient and robust landmark detection in volumetric data. In *International conference on medical image computing and computer-assisted intervention*, pages 565–572. Springer, 2015. 3

[54] Yi Zhou, Connelly Barnes, Jingwan Lu, Jimei Yang, and Hao Li. On the Continuity of Rotation Representations in Neural

Networks. In *Proceedings of CVPR*, page 9, Long Beach, CA, June 2019. IEEE. 5

[55] D. Zukić, J. Vicory, M. McCormick, L. Wisse, G. Gerig, P. Yushkevich, and S. Aylward. Nd morphological contour interpolation. 08 2016. 4, 12

## A. SDF Decoder Implementation

### A.1. Sampling SDF Coordinate/Value Pairs

As mentioned in the main body, to train the shape decoder we require coordinate/SDF value pairs in a canonical space. Since segmentation labels are almost always provided as voxelized masks, we must first remove the worst of the discretization effects. Because high inter-slice distances are a common issue, we first perform within-slice interpolation [1, 55] to a common 1mm inter-slice resolution. We then apply Gaussian smoothing using the PyMCubes [38] package to the masks, followed by marching cubes [23] to produce a good quality mesh. Since this produces an unnecessarily dense set of vertices, we reduce their number using Quadric smoothing [10]. We do this two times to produce two versions: one reduced by a factor of 10 and one by a factor of 100, constructing a simplified and extremely simplified version of each mesh, respectively. The next step is to rigidly align each mesh to an arbitrarily chosen anchor mesh (the first mesh in the training list) using coherent point drift [35, 18]. We use the extremely simplified mesh versions since it is much more computationally efficient. The computed rigid alignment parameters from the “extremely simplified” meshes are then used to align the “simplified” meshes.

We now have high-quality and aligned meshes, which are all scaled to fit in the unit sphere to create the canonical meshes. To sample SDF values from the meshes, we follow Park *et al.*’s [37] approach of randomly sampling within the unit sphere, with regions near the surface much more densely sampled. We use the mesh-to-sdf package [20], which recreates the sampling scheme of Park *et al.* [37], but we modify its settings. First, we sample a greater proportion of uniformly distributed points (20% of coordinate/SDF value pairs are sampled uniformly across the uniform sphere). The other 80% are sampled closer to the boundary by randomly selecting boundary points and jittering them randomly. Unlike Park *et al.* [37], we use higher magnitude jitters: either 0.1 or 0.01 (with equal probability) in normalized space. This sampling scheme allowed our shape decoder to converge much better than when using Park *et al.*’s settings. We sample 1 million coordinate/SDF value pairs per shape to train the SDF decoder.

### A.2. Training

For the most part, we follow Park *et al.*’s settings and hyper-parameters to train the shape decoder MLP. Namely,

Parameter	Value
$\sigma$	100
Batch Size	6
SDF Samples/Iteration	30000
$\mathcal{Z}$ Learning Rate	0.001
$\theta_S$ Learning Rate	0.0005
Epochs	2000
Latent Size	256
Dropout Probability	0.2
Optimizer	Adam [19]
Weight decay	0.0001

Table 4. Hyper-parameters for training the shape decoder

the MLP structure is a simple 8 layer MLP with 512 channels in each layer and dropout with 20% probability after each layer. The latent code is injected at the fourth layer. Weight normalization [42] is used after every layer as well. At every iteration and for every shape, 30 000 coordinate/SDF value pairs are randomly sampled from the list of 1 million to compute the loss. Like Park *et al.*, an equal proportion of positive and negative SDF values are sampled. Unlike Park *et al.* [37], we do not use a clamped loss, since the specific SDF values far away from the boundary are still useful for fitting pose. Table 4 lists the hyper-parameters, most of which follow Park *et al.* [37]. Note, after 1000 epochs, the learning rates were reduced by a factor of 10.

## B. Pose Encoder Implementation

### B.1. Sampling SDF Coordinate/Value Pairs

To train the pose encoders, coordinate/SDF value pairs need to be sampled in the image space, *i.e.*, not the canonical space. To do this, we first generate an SDF from the original masks [28]. Like for training the SDF decoder, we more densely sample closer to the shape boundary. We sample all coordinate/SDF value pairs from regions within 13 mm of the boundary (which corresponds to 10% of the canonical space after normalization). We divide these up into positive and negative SDF samples, and for each we add 10% more coordinate/SDF value pairs that are sampled uniformly across positive and negative regions of the entire SDF volume, respectively.

### B.2. Training

We use the encoder structure of Lee *et al.*’s [22] residual symmetric U-Net architecture to estimate the rigid and non-rigid pose parameters. The encoder structure has 4 residual blocks with max pooling after each block. We perform global average pooling after the final layer of the final residual block, resulting in a size-512 feature vector. We train all pose encoders with an initial learning rate 0.001 and with the Adam optimizer [19], which is reduced by a factor of 10 after each validation plateau. We truncate the im-

Parameter	Value
Batch Size (Translation)	8
Batch Size (Scale, Rotation, Non-Rigid)	12
Epochs (Translation)	65
Epochs (Scale)	80
Epochs (Rotation)	80
Epochs (non-rigid)	120
SDF Samples/Step	150000
$\sigma$ (Non-Rigid)	100
Model Learning Rate	0.001
Weight Decay	0.0001
T (Translation)	7
T (Scale, Rotation, Non-Rigid)	15

Table 5. Hyper-parameters for training DISSM

age intensity values of all scans to the range of  $[-160, 240]$  Hounsfield units (HU) to remove the irrelevant details. Table 5 lists other hyper parameters for training the DISSM pose encoders.

Following MSL procedures, we first train a translation encoder to predict the translation needed for the mean shape to fit the volume. To estimate translation pose, the model needs to see the entire volume so that the necessary adjustments can be made to move closer to the ground truth. Due to limited computational resources, we resample the volume to  $4 \times 4 \times 4$  mm resolution and symmetrically pad across the dimensions to create a unified volume size of physical dimension  $512 \times 512 \times 808$  mm, which is large enough to cover all volumes in the MSD training set. To allow DISSM to learn to provide pose corrections from a variety of translation trajectories, we perturb the prior pose at every episodic step by random values within a range of  $[-40, 40]$  mm using a uniform distribution.

Once the translation encoder is trained, we crop the resampled volume based on the translated mean shape. The cropped volume is then padded so that we cover enough area around the location to account for any changes in scale. Based on the dataset and a margin for safety, we crop the volume to a  $512 \times 432 \times 352$  mm area. The cropped volume is then used to train the scale, rotation, and non-rigid encoders. Focusing on scale first and similar to the translation model, we perturb the trajectory at every episodic step. However, following MSL principles, the translation perturbations are smaller in magnitude than before to focus the search space on scale. Additionally, we also randomly pick between “standard” and “fine-scale” ranges of perturbations. When the latter is picked, it helps sample more poses closer to the convergence point when the model is at the final steps of its episode. This allows the model to better learn when to stop producing corrections, ensuring it will converge to a pose in inference. We also clip the scale parameters to lie between  $[0.5, 2]$  and impose a penalty for

Parameter	Standard Range	Fine Range
Translation (mm)	$[-16, 16]$	$[-8, 8]$
Scale	$[0.7, 1.3]$	$[0.9, 1.1]$

Table 6. Perturbation ranges for training the scale encoder. The “standard” and “fine” ranges are randomly chosen at each step with 50% probability each. Values are then randomly sampled within the resulting ranges using a uniform distribution.

Parameter	Standard Range	Fine Range
Translation (mm)	$[-12, 12]$	$[-8, 8]$
Scale	$[0.97, 1.03]$	$[0.99, 1.01]$
Rotation (deg)	$[-7.5, 7.5]$	$[-4.5, 4.5]$

Table 7. Perturbation ranges for training the rotation encoder. The “standard” and “fine” ranges are randomly chosen at each step with 50% probability each. Values are then randomly sampled within the resulting ranges using a uniform distribution.

Parameter	Standard Range	Fine Range
Translation (mm)	$[-8, 8]$	$[-4, 4]$
Scale	$[0.99, 1.01]$	$[0.995, 1.015]$
Rotation (deg)	$[-4.5, 4.5]$	$[-2.5, 2.5]$

Table 8. Perturbation ranges for training the non-rigid encoder. The “standard” and “fine” ranges are randomly chosen at each step with 50% probability each. Values are then randomly sampled within the resulting ranges using a uniform distribution.

any scale predictions exceeding that range:

$$\max(0, s_{(.)} - 2) + \max(0, 0.5 - s_{(.)}), \quad (14)$$

where  $s_{(.)}$  is any of  $s_x$ ,  $s_y$ , or  $s_z$ . This regularization threshold is determined based on the distribution of scales in the training set, which are computed during the rigid alignment coherent point drift step of Sec. A.1. The perturbation hyper parameters for training the scale encoder can be seen in Table 6.

We follow the same procedure to train rotation and non-rigid encoders. The perturbation hyper parameters for training rotation and non-rigid encoders can be seen in Tables 7 and 8, respectively. Finally, we also perform image-based data augmentations such as random affine transformations, random Gaussian noise, random brightness changes, and random intensity shifts for all pose encoders.

## C. Training Local Refinement Model

Once the non-rigid model is trained, we generate the non-rigid SDF for each volume and in the original volume resolution. Because the SDF output from the shape decoder is not necessarily a proper SDF, we reinitialize it [43] using the ITK software [29]. To make the model robust to variations in the SDF, prior to generating each SDF we randomly add Gaussian noise with mean 0 and standard deviation 0.01 to the predicted latent vector. We generate 10 non-rigid SDFs for each volume this way, randomly choosing one SDF to pair with the image when training.

Parameter	Value
Batch Size	2
Epochs	150
Model Learning Rate	0.001
Weight decay	0.0001
$\lambda_1$	1
$\lambda_2$	0.1

Table 9. Hyper-parameters for training local refinement model

We follow the standard 3D U-Net architecture from [7] and input both the original volume along with randomly picked non-rigid SDF from the pool of SDFs for each volume. We further augment the SDF channels through small rigid random affine transformations that are independent of the image channel. We weight the loss with  $\lambda_1$  and  $\lambda_2$  in (13) using the values mentioned in Table 9. As mentioned in the main body, we only produce refinements within a narrow band of the non-rigid SDFs iso-boundary, which allows the model to focus only on the surface of the liver. We define the narrow band as being within 25 mm of the iso-boundary. Finally, we set the  $\rho$  in (13) to 12 mm. We apply standard data augmentations to both input channels, such as random affine transformations (both channels), and random shifting intensity, random Gaussian noise, and random brightness shifts (only image channel) while training the local refinement model.

## D. Competitor Methods

We compare DISSM with the competitor methods 2D PHNN [39], H-DenseUNet[24], nnU-Net (cascade)[17]. we follow the same procedure including the data preprocessing, data augmentation and post processing as mentioned in their respective papers. nnU-Net cascade preprocesses the image by resampling to the median voxel spacing. Third order spline interpolation is used for image data and nearest neighbour interpolation for label data. H-DenseUNet preprocesses the image by resampling to a fixed resolution  $0.69 \times 0.69 \times 1\text{mm}^3$  with the HU values clipped to  $[-200, 250]$ . For 2D PHNN, we use the original resolution and clip the HUs to  $[-200, 250]$ . For post processing, we select largest connected component for all the competitor methods coupled with 3D hole-filling.